

The VIMOS Public Extragalactic Redshift Survey (VIPERS) ^{*}

Exploring the dependence of the three-point correlation function on stellar mass and luminosity at $0.5 < z < 1.1$

M. Moresco^{1,2}, F. Marulli^{1,2,3}, L. Moscardini^{1,2,3}, E. Branchini^{4,5,6}, A. Cappi^{2,7}, I. Davidzon^{8,2}, B. R. Granett⁹, S. de la Torre⁸, L. Guzzo^{9,10}, U. Abbas¹¹, C. Adami⁸, S. Arnouts^{8,12}, J. Bel^{13,14}, M. Bolzonella², D. Bottini¹⁵, J. Coupon¹⁶, O. Cucciati², G. De Lucia¹⁷, P. Franzetti¹⁵, A. Fritz¹⁵, M. Fumana¹⁵, B. Garilli¹⁵, O. Ilbert⁸, A. Iovino⁹, J. Krywult¹⁸, V. Le Brun⁸, O. Le Fèvre⁸, K. Małek¹⁹, H. J. McCracken²⁰, M. Polletta¹⁵, A. Pollo^{19,21}, M. Scodreggio¹⁵, L. A. M. Tasca⁸, R. Tojeiro²², D. Vergani²³, and A. Zanichelli²⁴

(Affiliations can be found after the references)

Received –; accepted –

ABSTRACT

Aims. The three-point correlation function (3PCF) is a powerful probe to investigate the clustering of matter in the Universe in a complementary way with respect to lower-order statistics, providing additional information with respect to two-point correlation function and allowing to shed light on biasing, nonlinear processes and deviations from Gaussian statistics. In this paper, we analyse the first data release of the VIMOS Public Extragalactic Redshift Survey (VIPERS), determining the dependence of the three-point correlation function on luminosity and stellar mass at $z = [0.5, 1.1]$.

Methods. We exploit the VIPERS Public Data Release 1, consisting of more than 50000 galaxies with B-band magnitudes in the range $-21.6 \lesssim M_B - 5 \log(h) \lesssim -19.9$ and stellar masses in the range $9.8 \lesssim \log(M_* [h^{-2} M_\odot]) \lesssim 10.7$. We measure both the connected 3PCF and the reduced 3PCF in redshift space, probing different configurations and scales, in the range $2.5 < r [h^{-1} \text{Mpc}] < 20$.

Results. We find a significant dependence of the reduced 3PCF on scales and triangle shapes, with stronger anisotropy at larger scales ($r \sim 10 h^{-1} \text{Mpc}$) and an almost flat trend at smaller scales, $r \sim 2.5 h^{-1} \text{Mpc}$. Massive and luminous galaxies present a larger connected 3PCF, while the reduced 3PCF is remarkably insensitive to magnitude and stellar masses in the range we explored. These trends, already observed at low redshifts, are confirmed for the first time to be still valid up to $z = 1.1$.

Key words. Cosmology: observations – Cosmology: large-scale structure of Universe – Surveys – Galaxies: evolution

1. Introduction

The clustering of galaxies, and its evolution with cosmic time, is one of the major probes of modern cosmology. It provides crucial constraints on the underlying distribution of matter in the Universe, of which galaxies represent a biased tracer, and thus helps improve our knowledge of the fundamental components driving the evolution of the Universe. In particular, the two-point correlation function (2PCF) and its analogous in Fourier space, the power spectrum $P(k)$, have been extensively exploited as cosmological probes. Encoded in the shape

and amplitude of the 2-point statistics is the imprint of primordial fluctuations and their evolution in the pre- and post-recombination era, the most notable example of which are the baryonic acoustic oscillation (BAO) signature that, for the 2PCF, is in the form of a peak at a characteristic length scale that can provide an ideal “standard ruler”. Indeed, this feature has been exploited to place constraints on the expansion history of the Universe, measuring both the Hubble parameter $H(z)$ and the angular diameter distance $D_A(z)$, offering new insights on the nature of dark energy and dark matter (Eisenstein et al. 2005; Cole et al. 2005; Blake et al. 2011; Beutler et al. 2011; Anderson et al. 2012, 2014; Cuesta et al. 2016).

Galaxy clustering can provide useful information also to understand how galaxies have evolved with cosmic time. In particular, it has been found that more luminous and massive galaxies are more strongly clustered than fainter and less massive ones (Davis & Geller 1976; Davis et al. 1988; Hamilton 1988; Loveday et al. 1995; Benoist et al. 1996; Guzzo et al. 1997, 2000; Norberg et al. 2001, 2002; Zehavi et al. 2002, 2005, 2011; Brown et al. 2003; Abbas & Sheth 2006; Li et al. 2006; Swanson et al. 2008; Ross et al. 2011; Guo et al. 2013; Marulli et al. 2013); similar trends have been found also as a function of morphology and colours, for which galaxies with a rounder shape and redder show an enhanced clustering. The 2PCF is also often used to provide constraints on galaxy bias b ,

Send offprint requests to: M. Moresco
e-mail: michele.moresco@unibo.it

* Based on observations collected at the European Southern Observatory, Paranal, Chile under programs 182.A-0886 (LP) at the Very Large Telescope, and also based on observations obtained with MegaPrime/MegaCam, a joint project of CFHT and CEA/DAPNIA, at the Canada-France-Hawaii Telescope (CFHT), which is operated by the National Research Council (NRC) of Canada, the Institut National des Science de l’Univers of the Centre National de la Recherche Scientifique (CNRS) of France, and the University of Hawaii. This work is based in part on data products produced at TERAPIX and the Canadian Astronomy Data Centre as part of the Canada-France-Hawaii Telescope Legacy Survey, a collaborative project of NRC and CNRS. The VIPERS web site is <http://vipers.inaf.it/>.

which quantifies the excess in clustering of the selected sample with respect to the underlying dark matter; however, these estimates have to assume a fiducial cosmology, and are degenerate with the amplitude of linear matter density fluctuations quantified at $8 h^{-1} \text{ Mpc}$, σ_8 , of the assumed model.

While a Gaussian field can be completely described by its two-point statistics, to detect non-Gaussian signals, both of primordial type and induced by non-linear evolution of clustering, and to understand the evolution of matter beyond the linear approximation, it is necessary to study higher-order statistics. The first significant order above 2PCF and power spectrum is represented by the three-point correlation function (3PCF) and bispectrum $B(k)$ respectively. These functions provide complementary information with respect to lower-order statistics, and can be used in combination with them to break degeneracies between estimated cosmological parameters, such as galaxy bias and σ_8 . Many studies exploited both the evolutionary and cosmological information encoded in the three-point statistics, both in configuration space (e.g. Fry 1994; Frieman & Gaztanaga 1994; Jing & Boerner 1997; Jing & Börner 2004; Kayo et al. 2004; Gaztañaga & Scoccimarro 2005; Nichol et al. 2006; Ross et al. 2006; Kulkarni et al. 2007; McBride et al. 2011a,b; Marín 2011; Marín et al. 2013; Guo et al. 2014; Moresco et al. 2014; Guo et al. 2015) and in Fourier space (e.g. Fry & Seldner 1982; Matarrese et al. 1997; Verde et al. 1998, 2000; Scoccimarro 2000; Scoccimarro et al. 2001; Sefusatti & Scoccimarro 2005; Sefusatti & Komatsu 2007).

The aim of this paper is to push these investigations to higher redshifts. For this purpose, we analyse the VIPERS Public Data Release 1 (PDR-1) (Guzzo et al. 2014; Garilli et al. 2014), constraining the dependence of the 3PCF on stellar mass and luminosity. A similar analysis of the same dataset has been performed by Marulli et al. (2013) (hereafter M13), but for the 2PCF. This paper is intended as an extension of the analysis done in M13, exploiting the additional constraints that can be obtained from higher-order correlation functions. In particular, we focus our analysis on the non-linear/mildly non-linear evolution regime, since the size of the survey does not allow to probe those scales sensitive to possible primordial non-Gaussianities.

The paper is organized as follows. In Sect. 2 we present the VIPERS galaxy sample, and describe how it has been divided in stellar mass, luminosity and redshift sub-samples. In Sect. 3 we discuss how the 3PCF and its errors have been measured. Finally, in Sect. 4 we present our results, showing the dependence of the measured 3PCF on scales, triplet shapes, redshifts, luminosity and the stellar mass. In Appendix A, we provide information on the covariance matrices for our analysis

Throughout this paper, we adopt a standard flat Λ CDM cosmology, with $\Omega_M = 0.25$ and $h = H_0/100 = 0.73 \text{ km s}^{-1} \text{ Mpc}^{-1}$. Magnitudes are given in the AB system.

2. The data

VIPERS is a recently completed ESO Large Programme, which has measured spectroscopic redshifts for a complete sample with $0.5 < z \lesssim 1.2$. Its general aim has been to build a sample of the general galaxy population with a combination of volume [$\sim 5 \times 10^7 (h^{-1} \text{ Mpc})^3$] and spatial sampling [$10^{-2} - 10^{-3} h^3 \text{ Mpc}^{-3}$] comparable to state-of-the-art local surveys. Its science drivers are to provide at these redshifts reliable statistical measurements of ensemble properties of large-scale structure (as the power spectrum and redshift-space distortions), of the galaxy population (as the stellar mass function) and their combination (as

galaxy bias and the role of the environment). The VIPERS PDR-1 is extensively described in Guzzo et al. (2014) and Garilli et al. (2014). It has publicly released the measurements of the first 57204 redshifts of the survey, comprising 54756 galaxies and AGN, and 2448 stars. The survey targets have been selected from the Canada-France-Hawaii Telescope Legacy Survey Wide (CFHTLS-Wide) optical photometric catalogues (Mellier et al. 2008) over two fields, W1 and W4, covering in total $\sim 24 \text{ deg}^2$. The sample has been selected with a magnitude limit of $i_{AB} < 22.5$, and a $(u - g) - (r - i)$ colour cut to properly select the desired redshift range $z \geq 0.5$. VIPERS spectra have been measured with the low-resolution grism mounted on the VIMOS multi-object spectrograph at the ESO VLT (Le Fèvre et al. 2002, 2003), providing a moderate spectral resolution ($R = 230$) and a wavelength range of 5500-9500 Å.

Stellar masses and absolute magnitudes have been computed for the entire VIPERS sample with the public code HYPERZMASS (Bolzonella et al. 2000, 2010), which performs a fit to the spectral energy distribution (SED) of the galaxies. The B Buser filter has been considered to calculate the absolute magnitudes (Fritz et al. 2014). We refer to Davidzon et al. (2013) for a more extended discussion about the SED-fitting technique.

Among several other investigations, the VIPERS data have been used to estimate the relation between baryons and dark matter through the galaxy bias (M13, Di Porto et al. 2014; Cucciati et al. 2014; Cappi et al. 2015; Granett et al. 2015).

Following the approach of M13, we divide our sample in three equally spaced redshift ranges, $z \in [0.5, 0.7]$, $z \in [0.7, 0.9]$ and $z \in [0.9, 1.1]$. Each of them is further divided in subsamples with different thresholds in stellar mass, M_* , and B-band absolute magnitude, M_B . Specifically, we considered the same subsamples analysed by M13, with four different thresholds in stellar mass ($\log(M_* [h^{-2} M_\odot]) > 9, 9.5, 10, 10.5$) and five in absolute B magnitude ($M_B < -19.5, -20, -20.5, -21, -21.5$). The properties of the various samples are reported in Tables 1 and 2.

The luminosity-redshift and stellar mass-redshift relations for VIPERS PDR-1 galaxies are shown in Fig. 1. Flat thresholds in stellar mass have been considered, since many works confirmed a negligible evolution in M_* up to $z \sim 1$ (Pozzetti et al. 2007, 2010; Davidzon et al. 2013). On the contrary, the adopted thresholds in absolute magnitude have been constructed to follow the redshift evolution of galaxies, considering $M_B(z) =$

Table 1. Properties of the selected VIPERS sub-samples in threshold luminosity bins. Absolute magnitudes are quoted in units of $M_B(z = 1.1) - 5 \log(h)$.

redshift range	median redshift	magnitude range	median magnitude	N_{gal}
[0.5, 0.7]	0.62	< -19.5	-19.87	17473
[0.5, 0.7]	0.62	< -20.0	-20.15	12432
[0.5, 0.7]	0.62	< -20.5	-20.49	7472
[0.5, 0.7]	0.62	< -21.0	-20.86	3599
[0.5, 0.7]	0.62	< -21.5	-21.28	1236
[0.7, 0.9]	0.79	< -20.0	-20.41	14442
[0.7, 0.9]	0.80	< -20.5	-20.68	9469
[0.7, 0.9]	0.80	< -21.0	-21.05	4605
[0.7, 0.9]	0.80	< -21.5	-21.45	1619
[0.9, 1.1]	0.97	< -20.5	-21.00	5207
[0.9, 1.1]	0.98	< -21.0	-21.25	3477
[0.9, 1.1]	0.99	< -21.5	-21.65	1409

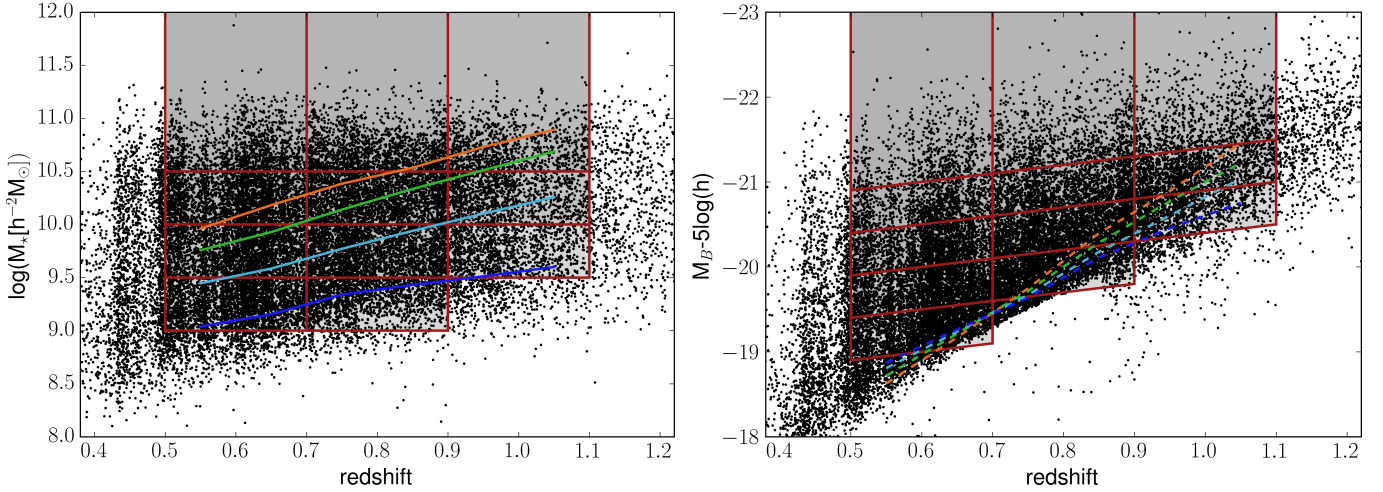


Fig. 1. Luminosity- and stellar mass-redshift relations. The black points represent VIPERS galaxies, where red boxes show the selected subsamples. The boxes in M_B absolute magnitude are constructed to follow the redshift evolution of galaxies, as discussed in the text. Coloured lines represent the 90% completeness limits for different sub-populations: orange lines for early-type galaxies, green for early-spirals, cyan for late spirals, and blue for irregulars and starbursts, respectively.

Table 2. Properties of the selected VIPERS sub-samples in threshold stellar mass bins. Stellar masses are quoted in units of $[h^{-2} M_{\star}]$.

redshift range	median redshift	stellar mass range	median stellar mass	N_{gal}
[0.5, 0.7]	0.61	> 9.0	9.82	17102
[0.5, 0.7]	0.62	> 9.5	10.11	11567
[0.5, 0.7]	0.62	> 10.0	10.35	6880
[0.5, 0.7]	0.62	> 10.5	10.66	2151
[0.7, 0.9]	0.78	> 9.0	9.93	15020
[0.7, 0.9]	0.79	> 9.5	10.15	11346
[0.7, 0.9]	0.79	> 10.0	10.39	6884
[0.7, 0.9]	0.79	> 10.5	10.67	2498
[0.9, 1.1]	0.97	> 9.5	10.19	4558
[0.9, 1.1]	0.97	> 10.0	10.46	2857
[0.9, 1.1]	0.97	> 10.5	10.71	1281

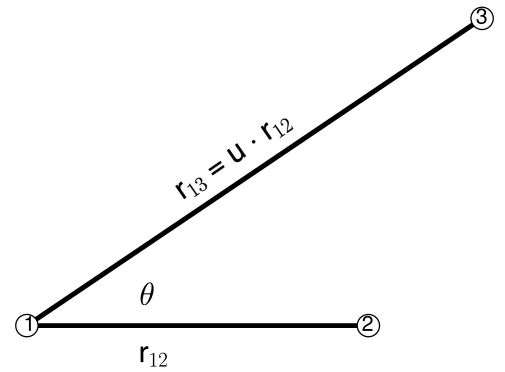


Fig. 2. The adopted parameterisation for estimating the 3PCF.

$M_B(0) + z$ (Ilbert et al. 2005; Zucca et al. 2009; Meneux et al. 2009; Fritz et al. 2014). Fig. 1 shows also the 90% completeness limits for different galaxy types. As it can be noted, all the magnitude-selected subsamples are volume-limited, except the ones in the lower redshift bins, where the reddest galaxies start to fall out of the VIPERS sample. On the other hand, mass incompleteness affects the subsamples selected in stellar mass. M13 performed a detailed analysis to quantitatively estimate this effect, finding a scale-dependent reduction of clustering that mainly affects very small scales ($\lesssim 1 h^{-1}$ Mpc), not significant for our analysis.

3. The three-point correlation function

3.1. Theoretical setup

The three-point correlation function estimates the probability of finding triplets of objects at relative comoving distances r_{12} , r_{13} , and r_{23} (Peebles 1980). If we define \bar{n} as the average density of objects, V_i as the comoving volumes at \vec{r}_i , and ξ as the two-point

correlation function, this probability can be written as:

$$dP = \bar{n}^3 [1 + \xi(r_{12}) + \xi(r_{13}) + \xi(r_{23}) + \zeta(r_{12}, r_{13}, r_{23})] dV_1 dV_2 dV_3. \quad (1)$$

From the connected 3PCF ζ it is possible to define also the reduced 3PCF as follows:

$$Q(r_{12}, r_{13}, r_{23}) \equiv \frac{\zeta(r_{12}, r_{13}, r_{23})}{\xi(r_{12})\xi(r_{13}) + \xi(r_{13})\xi(r_{23}) + \xi(r_{23})\xi(r_{13})}. \quad (2)$$

This function, introduced by Groth & Peebles (1977), has the advantage of having a smaller range of variation with respect to ξ and ζ , since it can be shown that in hierarchical scenarios $\zeta \propto \xi^2$ (Peebles & Groth 1975). Moreover it depends solely on the bias parameters, and not on σ_8 .

Different possible parameterisations have been discussed in literature to determine the triangles, in order to investigate the shape dependence of the 3PCF (Jing et al. 1995; Gaztañaga & Scoccimarro 2005; Nichol et al. 2006;

Kulkarni et al. 2007; Guo et al. 2014). In this paper, we adopt the parameterisation introduced by Marín (2011), in which the relation between two sides of the triangles is fixed, that is $r_{13} \equiv u \cdot r_{12}$, and then the 3PCF is estimated as a function of the angle θ between the two sides:

$$\begin{cases} r_{12} \\ r_{13} \equiv u \cdot r_{12} \\ r_{23} \equiv r_{12} \cdot \sqrt{1 + u^2 - 2 \cdot u \cdot \cos \theta}. \end{cases}$$

In this way, *elongated* configurations are represented by $\theta \sim 0$ and $\theta \sim \pi$, while *perpendicular* configurations by $\theta \sim \pi/2$ (see Fig. 2). Differently from other parameterisations, in which e.g. all the triangle sides are fixed and the 3PCF is only measured as a function of scale, the adopted configuration is particularly convenient to study at the same time the scale dependence of the 3PCF, by changing the length and the ratios between the first two triangle sides, and the shape dependence, as a function of the angle θ . As in Marín (2011), we consider a constant logarithmic binning in $\Delta r_{ij}/r_{ij}$. It has been demonstrated that this binning scheme allows one to include in each θ -bin triangles with similar shapes, providing also smaller errors with respect to other parameterisations.

3.2. Estimator and implementation

The Szapudi & Szalay (1998) estimator is used to measure the 3PCF:

$$\zeta(r_{12}, u \cdot r_{12}, \theta) = \frac{DDD - 3DDR + 3DRR - RRR}{RRR}, \quad (3)$$

where DDD , RRR , DDR , and DRR are the normalised numbers of data triplets, random triplets, data-data-random triplets, and data-random-random triplets respectively. The 2PCF is measured with the Landy & Szalay (1993) estimator:

$$\xi(r) = \frac{DD - 2DR + RR}{RR}, \quad (4)$$

where DD , RR and DR are the normalised numbers of data pairs, random pairs, and data-random pairs respectively.

To measure both the 2PCF and the 3PCF we exploit the CosmoBolognaLib, a large suite of C++ libraries for cosmological calculations (Marulli et al. 2016)¹. Pair and triplet counts are computed with a *chain-mesh* algorithm, that allows us to significantly reduce the CPU time by optimizing the search in the surveyed volume. Specifically, as a first step of the procedure, both the data and random catalogues are pixelized, that is they are divided in small sub-regions, and the indices of the objects belonging to each sub-region are stored in vectors. Then, the count is computed by running the algorithm only on the sub-regions actually contributing to the pair and triplet counts in the chosen scale range.

The random sample for each stellar mass and luminosity bin has been created implementing the same observing strategy of real data, with $N_R = 60N_{\text{gal}}$, where N_R is the number of random objects and N_{gal} is the number of galaxies in each sample. The redshifts of the random objects are drawn by the observed radial distribution of the W1+W4 VIPERS samples, conveniently smoothed as described in M13.

¹ The CosmoBolognaLib can be freely downloaded at <https://github.com/federicomarulli/CosmoBolognaLib>.

3.3. Error and weight estimate

We estimate the errors on the measured 3PCF using the set of 26 mock galaxy catalogues used in M13, and described in de la Torre et al. (2013). Halo Occupation Distribution (HOD) mocks calibrated on the real data are used for the luminosity-selected samples, while mocks implementing the stellar-to-halo mass relation (SHMR) of Moster et al. (2013) are used for the stellar mass-selected samples (de la Torre et al. 2013). In both cases, galaxies are assigned to dark matter haloes extracted from the MultiDark N-body simulation (Prada et al. 2012). To populate the simulation with haloes below the mass resolution limit, in order to reach the haloes hosting the very faint VIPERS galaxies, we exploit the technique described in de la Torre & Peacock (2013).

The covariance error matrix is estimated from the dispersion among the mock catalogues:

$$C_{ij} = \frac{1}{N} \sum_{k=1}^{N-1} (\mathcal{Q}_i^k - \bar{\mathcal{Q}}_i)(\mathcal{Q}_j^k - \bar{\mathcal{Q}}_j), \quad (5)$$

where $\bar{\mathcal{Q}}_j$ is the mean value of the reduced 3PCF averaged between the 26 mock catalogue. The errors on the 3PCF are then obtained from the square root of the diagonal values only of the covariance matrix, $\sigma_i = \sqrt{C_{ii}}$, applying on mock subsamples the selection criteria used on real data. Analogously, also the covariance error matrix for the connected 3PCF is estimated. Further information regarding the covariance matrices can be found in Appendix A. Given the limited number of mocks available, we consider only the diagonal elements of C_{ij} , and discuss in the Appendix the effect of considering the full covariance.

Following the same procedure described in M13, we apply to each galaxy a weight that depends on both its redshift, z , and position in the quadrant, Quad, given by:

$$w(\text{Quad}, z) = w_{TSR}(\text{Quad}) \cdot w_{SSR}(\text{Quad}) \cdot w_{CSR}(z),$$

and that accounts for three independent sources of systematic errors, each one quantified by its own weight:

- w_{TSR} is the weight that accounts for the target sampling rate, i.e. the probability that a galaxy in the photometric catalogue has a spectroscopic redshift measurement, and it is computed as the ratio between the total number of galaxies in the photometric catalogue and the ones actually spectroscopically targeted;
- w_{SSR} is the weight that accounts for the spectroscopic success rate, i.e. the probability that a galaxy spectroscopically targeted has a reliable redshift measurement, that is a redshift with flag $2 \leq z_{\text{flag}} \leq 9.5$ (for a more detailed discussion on VIPERS redshift flags, we refer to Guzzo et al. 2014);
- $w_{CSR}(z)$ is the weight that accounts for the colour sampling rate, defined as $CSR(z) = 0.5[1 - \text{erf}(7.405 - 17.465 \cdot z)]$, and taking into account the incompleteness due to the VIPERS colour selection.

Both w_{TSR} and w_{SSR} mainly depend on the quadrant Quad and on the redshift z , with all other possible dependencies being negligible (de la Torre et al. 2013). We verified that these weights do not significantly affect our results, typically changing the clustering measurements below the estimated 1σ uncertainties.

4. Results

In this section, we present the measurements of the redshift-space 3PCF for the VIPERS sample, discussing their depen-

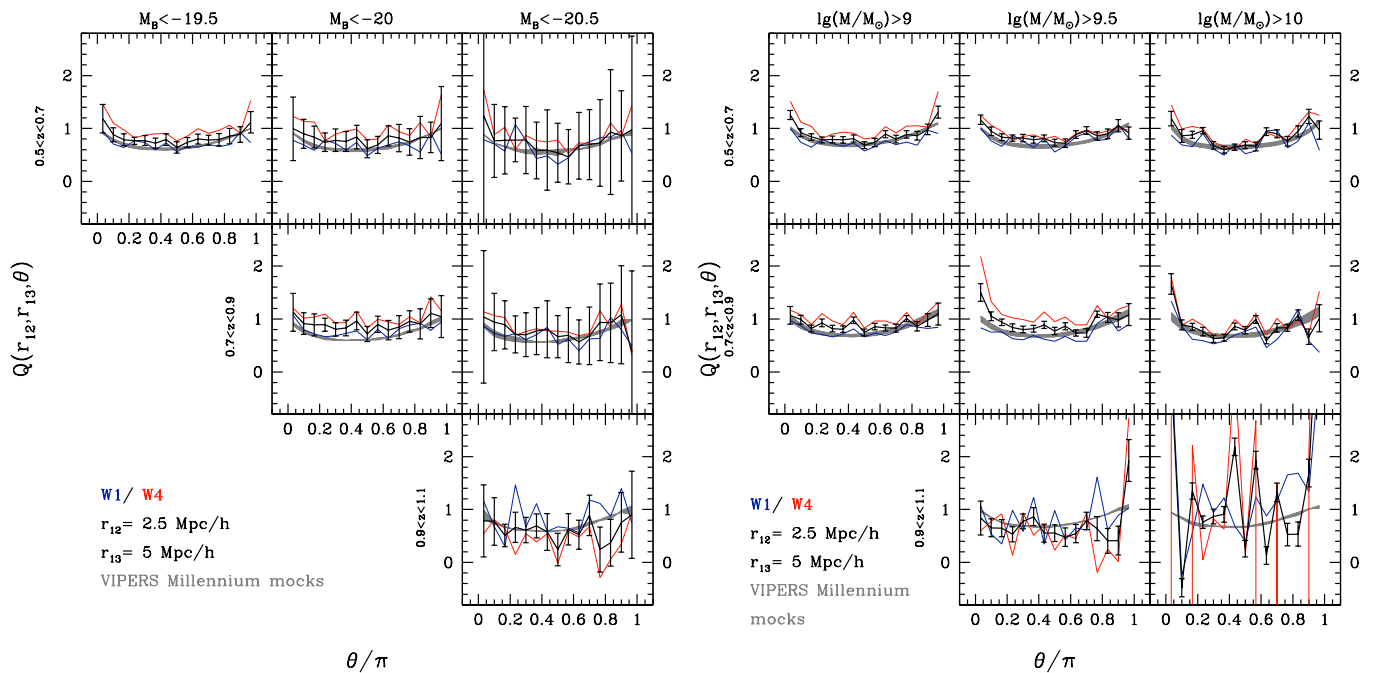


Fig. 3. Redshift-space reduced 3PCF, $Q(\theta)$, as a function of redshift (panels from top to bottom) for different luminosity (left plots) and stellar mass thresholds (right plots), for scales $r_{12} = 2.5 h^{-1} \text{Mpc}$ and $r_{13} = 5 h^{-1} \text{Mpc}$. Blue and red lines show the measurements in the W1 and W4 fields, respectively, while the black lines show the combined 3PCF, with its associated errors. The grey shaded area shows the redshift-space 3PCF measured in two large Millennium mock catalogues, constructed to mimic the properties of VIPERS data, and is not representative of the expected scatter on the theoretical measurements.

dence on shape, redshift, stellar mass and luminosity in comparison with what found in literature. The analysis has been performed both in W1 and W4 separately, and combining the counts in the two fields to provide a single measurement. The 3PCF has been measured in various redshift, stellar mass and luminosity bins, as discussed in Sect. 2. Differently from M13, we will show and discuss here only the results for the three lowest stellar mass and luminosity samples, since the most extreme bins result to be noise-dominated (namely $M_B < -21$, -21.5 and $\log(M_\star [h^{-2} M_\odot]) > 10.5$).

To explore the dependence of the clustering also on the scales and shapes of galaxy triplets, we analyse three different scales, with $r_{12} = 2.5, 5, 10 h^{-1} \text{Mpc}$. Throughout this analysis, we consider a ratio between the first and the second side of the triplet $r_{13} = 2 \cdot r_{12}$, and for each of these configurations we use 15 equi-spaced angular bins in θ . The high galaxy number density in VIPERS allows us to explore the 3PCF down to scales smaller than other surveys at similar redshift (e.g. WiggleZ, Marín et al. 2013). The choice of $r_{13}/r_{12} = 2$ is justified to avoid having strongly non-linear configurations that would appear in collapsed triangles for $r_{13}/r_{12} = 1$, and to allow comparison with similar analyses in literature (Marín 2011; McBride et al. 2011b; Marín et al. 2013).

4.1. Redshift and scale dependence

Figures 3, 4 and 5 show the redshift-space reduced 3PCF as a function of luminosity and stellar mass, in three redshift ranges and for three different configurations, for $r_{12} = 2.5, 5, 10 h^{-1} \text{Mpc}$ respectively. Both the 3PCF of W1 and W4 fields and the combined 3PCF are shown.

This analysis is in qualitative agreement with many previous works performed on both numerical simula-

tions (Gaztañaga & Scoccimarro 2005; Marín et al. 2008; Moresco et al. 2014) and real data (McBride et al. 2011b; Marín 2011; Marín et al. 2013; Guo et al. 2014), where it is found a transition from the “U” shape of $Q(\theta)$ to the “V” shape moving from the smaller to the larger scales. This feature indicates a more pronounced anisotropy in $Q(\theta)$ at increasing scales which is theoretically expected. It is related to the different shapes of structures at different scales, with compact, spherically symmetric structures dominating at small distances, and filamentary structures starting to contribute at larger scales, as indicated by the larger value of $Q(\theta)$ in the elongated configurations.

At small scales no significant evolution with redshift is found. However, in these configurations $Q(\theta)$ is generally flatter, and differences are harder to be detected. On the contrary, at larger scales it is possible to see a clear trend, with the 3PCF being flatter at higher redshifts. This can be interpreted as an indication of the build-up of filaments with cosmic time, that evolve enhancing the 3PCF in elongated configurations, while reducing it in the equilateral ones.

4.2. Luminosity and stellar mass dependence

In Figs. 6 and 7 we show the stellar mass and luminosity dependence in redshift space for both the connected and the reduced 3PCF, at the various scales explored in this analysis. In particular, we focus on the lower redshift range, $0.5 < z < 0.7$, where we have a larger leverage in observed properties.

In general, the connected 3PCF $\zeta(\theta)$ exhibits a much stronger dependence on both stellar mass and luminosity than the reduced 3PCF $Q(\theta)$, particularly evident at small scales. This differential trend in Q and ζ agrees with what found by Guo et al. (2014) from the analysis of a more local sample extracted from the SDSS-DR7. This effect can be explained con-

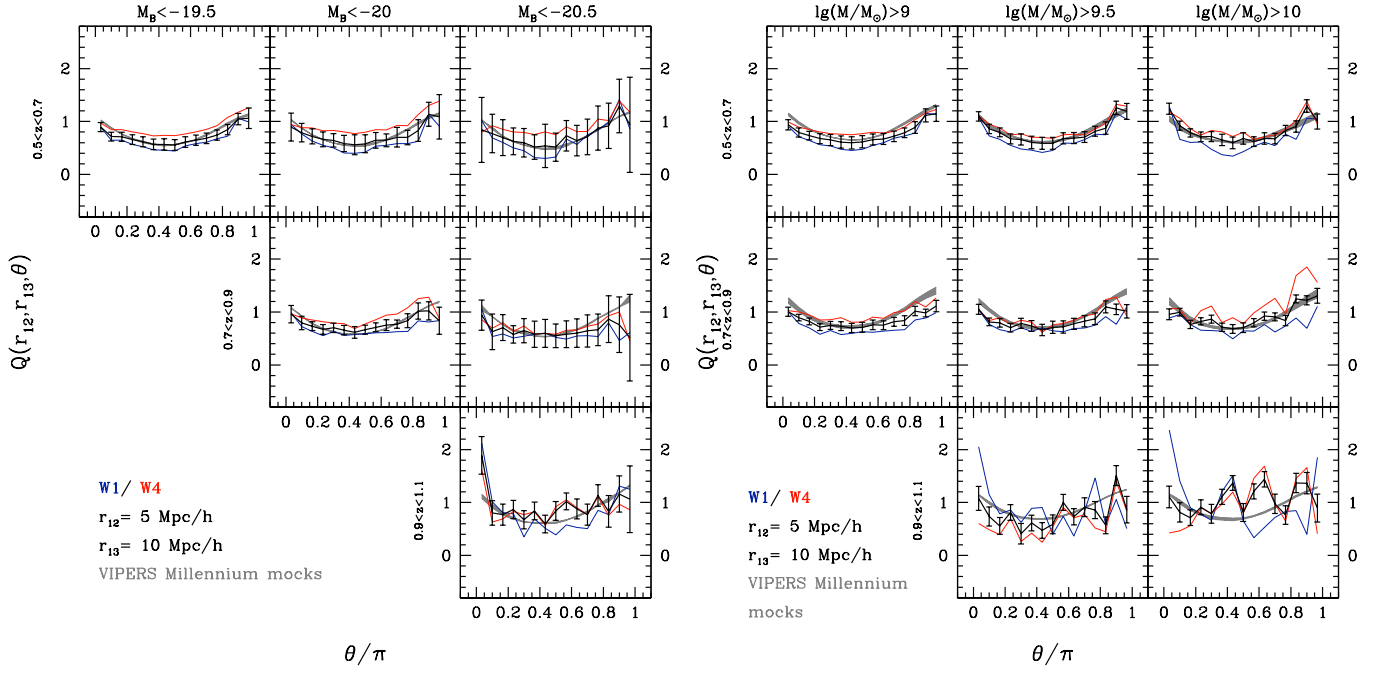


Fig. 4. Same as Fig. 3, but for scales $r_{12} = 5 h^{-1}$ Mpc and $r_{13} = 10 h^{-1}$ Mpc.

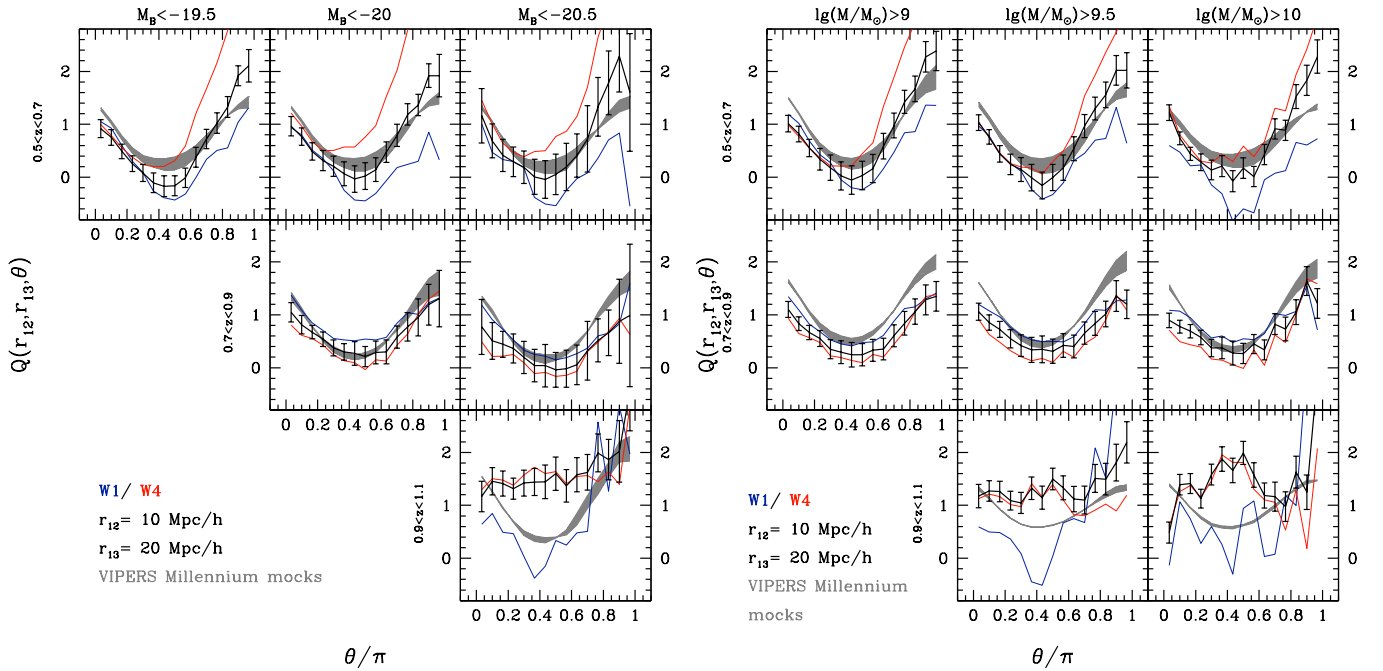


Fig. 5. Same as Fig. 3, but for scales $r_{12} = 10 h^{-1}$ Mpc and $r_{13} = 20 h^{-1}$ Mpc.

sidering the different sensitivity of the two functions on the bias parameters. According to second-order perturbation theory and in the hypothesis of linear bias (Fry & Gaztanaga 1993; Frieman & Gaztanaga 1994), the 2PCF of dark matter can be connected to the one of galaxies through the bias parameter b_1 , with a relation $\xi_g = b_1^2 \xi_m$; similarly, for the 3PCF it is possible to derive the relation $\zeta_g \sim b_1^3 \zeta_m$, that is valid at the first order. Hence, from Eq. 2 we have that $Q \propto 1/b_1$, and therefore the dependence of ζ on the linear bias is more significant. While our analysis finds a detectable trend in ζ , Q shows no significant trend neither in stellar mass nor in luminosity, in

contrast with some earlier results that find a slight dependence with luminous and massive galaxies having lower amplitudes of Q (Jing & Börner 2004; McBride et al. 2011b; Guo et al. 2014). The absence of any significant trend in our measurements can be due to the different redshift ranges probed. While most of previous works focused on local galaxies ($z < 0.3$), our analysis has been performed at $z > 0.5$, where the amplitude of the clustering and the non-Gaussianity due to non-linear evolution is smaller, reducing the differences in Q . Moreover, the fact that no dependence on luminosity or stellar mass is detectable in Q , despite the presence on a non-zero b_1 (as shown by the analysis of the

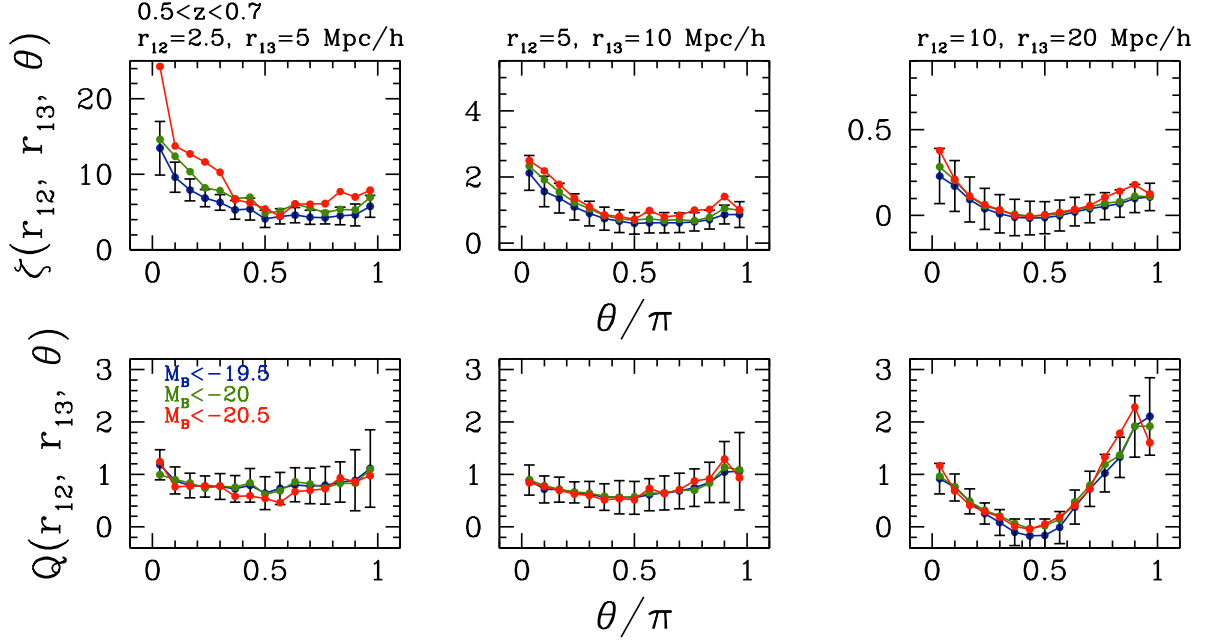


Fig. 6. Redshift-space connected 3PCF (upper panels) and reduced 3PCF (lower panels) as a function of luminosity at redshift $0.5 < z < 0.7$ for different scales. Different colours show the measurements in the lower (blue), intermediate (green), and higher (red) threshold bins. For clarity reason, errorbars are shown only in the lower bin.

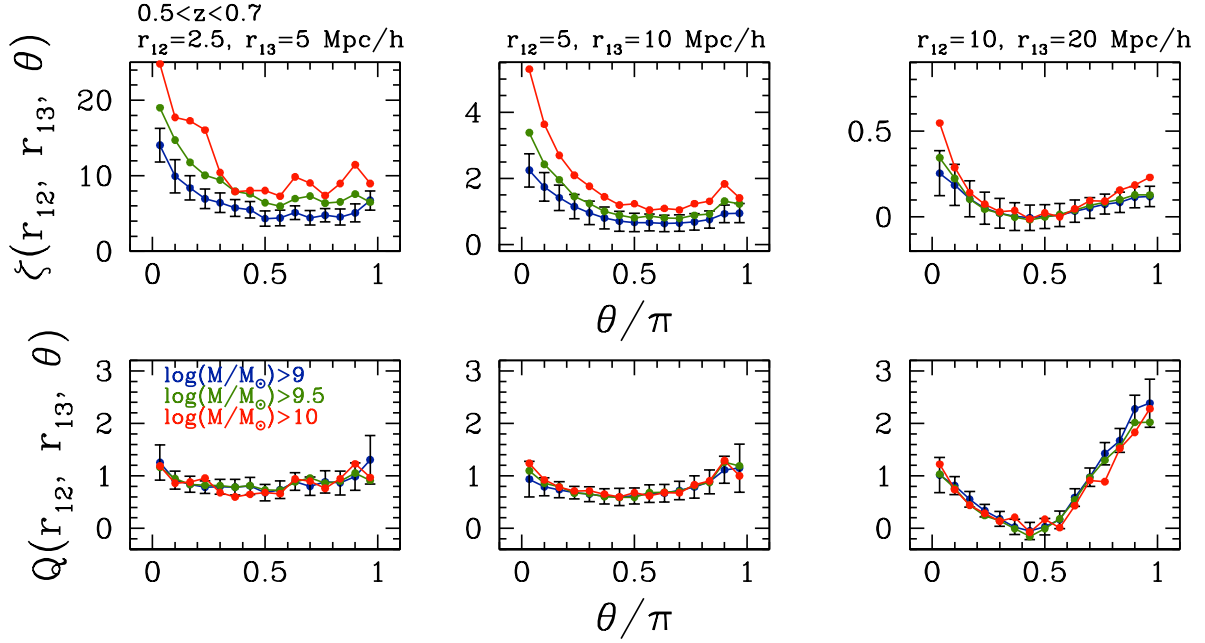


Fig. 7. Same as Fig. 6, but as a function of stellar mass.

2PCF on the same dataset, see M13) implies that a non-linear contribution to the bias should be present.

From the analysis of the 3PCF it can be found that more luminous and massive galaxies present a higher clustering, in agreement with the results obtained on the same sample from the 2PCF by M13. The larger dependence at smaller scales is confirming also the results found by Guo et al. (2014) from the anal-

ysis of SDSS-DR7. Cappi et al. (2015) also analysed VIPERS data, measuring volume-averaged higher-order correlation functions. A direct comparison of the results is not straightforward, since in their analysis they measured the galaxy normalised skewness S_3 , which, in hierarchical models, corresponds to $S_3 \sim 3Q$; however, this function is insensitive to spatial configuration, and any shape dependence is washed out. Nevertheless, both S_3

and Q quantify the contribution to higher-order correlation functions, and similarly a negligible dependence on luminosity was found.

4.3. Comparison with semi-analytic models

In Figs. 3, 4 and 5, we compare our measurements with theoretical expectations. Specifically, we consider mock galaxy catalogues constructed on top of the Millennium simulation (Springel et al. 2005), by using the Munich semi-analytic model (Blaizot et al. 2005; De Lucia & Blaizot 2007). The same stellar mass and luminosity thresholds used for real data (see Sect. 2) have been applied to select mock galaxy samples.

As it can be noted, there is a general agreement between our measurements and theoretical predictions, except in the higher redshift bins. Similar results have been found also for the 2PCF (Marulli et al. 2013). The results shown here extend that analysis to higher-order clustering. Assuming a local bias scenario, the 3PCF of dark matter can be connected to the one of galaxies following the equation $Q_g = 1/b_1(Q_{dm} + b_2/b_1)$, where b_1 is the linear bias parameter and b_2 the non-linear one. At the smallest scales (Fig. 3) the mocks tend to present a smaller normalization of Q for all redshifts and luminosities, except in the highest redshift bins, which can be interpreted in theoretical models failing to exactly reproduce the non-linear part of the evolution.

At larger scales ($r_{12}=5 h^{-1}$ Mpc, Fig. 4) the agreement with data is better, while at the largest probed scales (Fig. 5) the mocks tend not to reproduce the θ -dependence of Q , that may point to an inconsistency with the observed linear bias. The significance of this discrepancy, however, might be reduced once the full covariance error matrix is taken into account, which appear particularly relevant at the larger scales (see Appendix A).

5. Summary and conclusions

In this paper, we investigated the dependence of higher-order clustering on stellar mass and luminosity, providing measurements for the first time at high redshift ($z \sim 1$). We analysed galaxy samples extracted from VIPERS PDR-1, in the redshift range $0.5 < z < 1.1$, measuring both the connected and the reduced 3PCF in redshift space at different scales. The associated errors have been estimated from HOD and SHMR mock catalogues, specifically constructed to reproduce VIPERS observational properties.

We provided measurements of the connected and reduced 3PCF as a function of redshift, stellar mass and luminosity for three different scales, $r_{12} = 2.5, 5, 10 h^{-1}$ Mpc and $r_{13} = 2 \cdot r_{12}$, mapping from small to intermediate scales.

The main results of this work can be summarised as follows:

- We find a strong dependence of the reduced 3PCF on scales at all redshifts and for all stellar mass and luminosity bins, with an almost flat $Q(\theta)$ at smaller scales and a more prominent anisotropy at larger scales ($r_{12} = 10 h^{-1}$ Mpc) independently of the redshift. This trend can be interpreted as a signature of an increasing contribution of filamentary structures in the correlation function.
- From the analysis of the connected 3PCF $\zeta(\theta)$, we find that more massive and luminous galaxies present a stronger clustering, confirming the results obtained at lower redshifts in SDSS and extending them, for the first time, up to $z \sim 1.1$.
- The analysis of $Q(\theta)$ as a function of stellar mass and luminosity presents results with smaller statistical significance, in agreement with the results of previous studies.

In a forthcoming paper we will take advantage of the higher statistics provided by VIPERS final release to improve our constraints on the 3PCF, and to extract information on the galaxy bias independently of the measurements obtained with other techniques (e.g. the 2PCF), that usually have to assume a cosmological model.

Acknowledgments

We acknowledge the crucial contribution of the ESO staff for the management of service observations. In particular, we are deeply grateful to M. Hilker for his constant help and support of this program. Italian participation to VIPERS has been funded by INAF through PRIN 2008 and 2010 programs. LG and BRG acknowledge support of the European Research Council through the Darklight ERC Advanced Research Grant (# 291521). OLF acknowledges support of the European Research Council through the EARLY ERC Advanced Research Grant (# 268107). AP, KM, and JK have been supported by the National Science Centre (grants UMO-2012/07/B/ST9/04425 and UMO-2013/09/D/ST9/04030), the Polish-Swiss Astro Project (co-financed by a grant from Switzerland, through the Swiss Contribution to the enlarged European Union). KM was supported by the Strategic Young Researcher Overseas Visits Program for Accelerating Brain Circulation No. R2405. RT acknowledge financial support from the European Research Council under the European Community's Seventh Framework Programme (FP7/2007-2013)/ERC grant agreement n. 202686. MM, EB, FM and LM acknowledge the support from grants ASI-INAF I/023/12/0 and PRIN MIUR 2010-2011. LM also acknowledges financial support from PRIN INAF 2012. Research conducted within the scope of the HECOLS International Associated Laboratory, supported in part by the Polish NCN grant DEC-2013/08/M/ST9/00664.

References

- Abbas, U. & Sheth, R. K. 2006, Mon. Not. R. Astron. Soc., 372, 1749
- Anderson, L., Aubourg, E., Bailey, S., et al. 2012, Mon. Not. R. Astron. Soc., 427, 3435
- Anderson, L., Aubourg, É., Bailey, S., et al. 2014, Mon. Not. R. Astron. Soc., 441, 24
- Benoist, C., Maurogordato, S., da Costa, L. N., Cappi, A., & Schaeffer, R. 1996, *Astrophys. J.*, 472, 452
- Beutler, F., Blake, C., Colless, M., et al. 2011, Mon. Not. R. Astron. Soc., 416, 3017
- Blaizot, J., Wadadekar, Y., Guiderdoni, B., et al. 2005, Mon. Not. R. Astron. Soc., 360, 159
- Blake, C., Kazin, E. A., Beutler, F., et al. 2011, Mon. Not. R. Astron. Soc., 418, 1707
- Bolzonella, M., Kovač, K., Pozzetti, L., et al. 2010, *Astron. Astrophys.*, 524, A76
- Bolzonella, M., Miralles, J.-M., & Pelló, R. 2000, *Astron. Astrophys.*, 363, 476
- Brown, M. J. I., Dey, A., Jannuzi, B. T., et al. 2003, *Astrophys. J.*, 597, 225
- Cappi, A., Marulli, F., Bel, J., et al. 2015, *Astron. Astrophys.*, 579, A70
- Cole, S. et al. 2005, Mon. Not. R. Astron. Soc., 362, 505
- Cucciati, O., Granett, B. R., Branchini, E., et al. 2014, *Astron. Astrophys.*, 565, A67
- Cuesta, A. J., Vargas-Magaña, M., Beutler, F., et al. 2016, Mon. Not. R. Astron. Soc., 457, 1770
- Davidzon, I., Bolzonella, M., Coupon, J., et al. 2013, *Astron. Astrophys.*, 558, A23
- Davis, M. & Geller, M. J. 1976, *Astrophys. J.*, 208, 13
- Davis, M., Meiksin, A., Strauss, M. A., da Costa, L. N., & Yahil, A. 1988, *Astrophys. J. Lett.*, 333, L9
- de la Torre, S., Guzzo, L., Peacock, J. A., et al. 2013, *Astron. Astrophys.*, 557, A54
- de la Torre, S. & Peacock, J. A. 2013, Mon. Not. R. Astron. Soc., 435, 743
- De Lucia, G. & Blaizot, J. 2007, Mon. Not. R. Astron. Soc., 375, 2
- Di Porto, C., Branchini, E., Bel, J., et al. 2014, arXiv:1406.6692

Eisenstein, D. J. et al. 2005, *Astrophys. J.*, 633, 560
Frieman, J. A. & Gaztanaga, E. 1994, *Astrophys. J.*, 425, 392
Fritz, A., Scodreggio, M., Ilbert, O., et al. 2014, *Astron. Astrophys.*, 563, A92
Fry, J. N. 1994, *Physical Review Letters*, 73, 215
Fry, J. N. & Gaztanaga, E. 1993, *Astrophys. J.*, 413, 447
Fry, J. N. & Seldner, M. 1982, *Astrophys. J.*, 259, 474
Garilli, B., Guzzo, L., Scodreggio, M., et al. 2014, *Astron. Astrophys.*, 562, A23
Gaztañaga, E. & Scoccimarro, R. 2005, *Mon. Not. R. Astron. Soc.*, 361, 824
Granett, B. R., Branchini, E., Guzzo, L., et al. 2015, *Astron. Astrophys.*, 583, A61
Groth, E. J. & Peebles, P. J. E. 1977, *Astrophys. J.*, 217, 385
Guo, H., Li, C., Jing, Y. P., & Börner, G. 2014, *Astrophys. J.*, 780, 139
Guo, H., Zehavi, I., Zheng, Z., et al. 2013, *Astrophys. J.*, 767, 122
Guo, H., Zheng, Z., Jing, Y. P., et al. 2015, *Mon. Not. R. Astron. Soc.*, 449, L95
Guzzo, L., Bartlett, J. G., Cappi, A., et al. 2000, *Astron. Astrophys.*, 355, 1
Guzzo, L., Scodreggio, M., Garilli, B., et al. 2014, *Astron. Astrophys.*, 566, A108
Guzzo, L., Strauss, M. A., Fisher, K. B., Giovanelli, R., & Haynes, M. P. 1997, *Astrophys. J.*, 489, 37
Hamilton, A. J. S. 1988, *Astrophys. J. Lett.*, 331, L59
Hoffmann, K., Bel, J., Gaztañaga, E., et al. 2015, *Mon. Not. R. Astron. Soc.*, 447, 1724
Ilbert, O., Tresse, L., Zucca, E., et al. 2005, *Astron. Astrophys.*, 439, 863
Jing, Y. P. & Boerner, G. 1997, *Astron. Astrophys.*, 318, 667
Jing, Y. P. & Börner, G. 2004, *Astrophys. J.*, 607, 140
Jing, Y. P., Börner, G., & Valdarnini, R. 1995, *Mon. Not. R. Astron. Soc.*, 277, 630
Kayo, I., Suto, Y., Nichol, R. C., et al. 2004, *Publ. Astron. Soc. Japan*, 56, 415
Kulkarni, G. V., Nichol, R. C., Sheth, R. K., et al. 2007, *Mon. Not. R. Astron. Soc.*, 378, 1196
Landy, S. D. & Szalay, A. S. 1993, *Astrophys. J.*, 412, 64
Le Fèvre, O., Mancini, D., Saisse, M., et al. 2002, *The Messenger*, 109, 21
Le Fèvre, O., Saisse, M., Mancini, D., et al. 2003, in *Society of Photo-Optical Instrumentation Engineers (SPIE) Conference Series*, Vol. 4841, Society of Photo-Optical Instrumentation Engineers (SPIE) Conference Series, ed. M. Iye & A. F. M. Moorwood, 1670–1681
Li, C., Kauffmann, G., Jing, Y. P., et al. 2006, *Mon. Not. R. Astron. Soc.*, 368, 21
Loveday, J., Maddox, S. J., Efstathiou, G., & Peterson, B. A. 1995, *Astrophys. J.*, 442, 457
Marín, F. 2011, *Astrophys. J.*, 737, 97
Marín, F. A., Blake, C., Poole, G. B., et al. 2013, *Mon. Not. R. Astron. Soc.*, 432, 2654
Marín, F. A., Wechsler, R. H., Frieman, J. A., & Nichol, R. C. 2008, *Astrophys. J.*, 672, 849
Marulli, F., Bolzonella, M., Branchini, E., et al. 2013, *Astron. Astrophys.*, 557, A17
Marulli, F., Veropalumbo, A., & Moresco, M. 2016, *Astronomy and Computing*, 14, 35
Matarrese, S., Verde, L., & Heavens, A. F. 1997, *Mon. Not. R. Astron. Soc.*, 290, 651
McBride, C. K., Connolly, A. J., Gardner, J. P., et al. 2011a, *Astrophys. J.*, 739, 85
McBride, C. K., Connolly, A. J., Gardner, J. P., et al. 2011b, *Astrophys. J.*, 726, 13
Mellier, Y., Bertin, E., Hudelot, P., et al. 2008, <http://terapix.iap.fr/cpl/oldSite/Descart/CFHTLS-T0005-Release.pdf>
Meneux, B., Guzzo, L., de la Torre, S., et al. 2009, *Astron. Astrophys.*, 505, 463
Moresco, M., Marulli, F., Baldi, M., Moscardini, L., & Cimatti, A. 2014, *Mon. Not. R. Astron. Soc.*, 443, 2874
Moster, B. P., Naab, T., & White, S. D. M. 2013, *Mon. Not. R. Astron. Soc.*, 428, 3121
Nichol, R. C., Sheth, R. K., Suto, Y., et al. 2006, *Mon. Not. R. Astron. Soc.*, 368, 1507
Norberg, P., Baugh, C. M., Hawkins, E., et al. 2002, *Mon. Not. R. Astron. Soc.*, 332, 827
Norberg, P., Baugh, C. M., Hawkins, E., et al. 2001, *Mon. Not. R. Astron. Soc.*, 328, 64
Peebles, P. J. E. 1980, *The large-scale structure of the universe*
Peebles, P. J. E. & Groth, E. J. 1975, *Astrophys. J.*, 196, 1
Pozzetti, L., Bolzonella, M., Lamareille, F., et al. 2007, *Astron. Astrophys.*, 474, 443
Pozzetti, L., Bolzonella, M., Zucca, E., et al. 2010, *Astron. Astrophys.*, 523, A13
Prada, F., Klypin, A. A., Cuesta, A. J., Betancort-Rijo, J. E., & Primack, J. 2012, *Mon. Not. R. Astron. Soc.*, 423, 3018
Ross, A. J., Brunner, R. J., & Myers, A. D. 2006, *Astrophys. J.*, 649, 48
Ross, A. J., Tojeiro, R., & Percival, W. J. 2011, *Mon. Not. R. Astron. Soc.*, 413, 2078
Scoccimarro, R. 2000, *Astrophys. J.*, 544, 597

Scoccimarro, R., Feldman, H. A., Fry, J. N., & Frieman, J. A. 2001, *Astrophys. J.*, 546, 652
Sefusatti, E. & Komatsu, E. 2007, *Phys. Rev. D*, 76, 083004
Sefusatti, E. & Scoccimarro, R. 2005, *Phys. Rev. D*, 71, 063001
Springel, V. et al. 2005, *Nature*, 435, 629
Swanson, M. E. C., Tegmark, M., Blanton, M., & Zehavi, I. 2008, *Mon. Not. R. Astron. Soc.*, 385, 1635
Szapudi, I. & Szalay, A. S. 1998, *Astrophys. J. Lett.*, 494, L41
Verde, L., Heavens, A. F., & Matarrese, S. 2000, *Mon. Not. R. Astron. Soc.*, 318, 584
Verde, L., Heavens, A. F., Matarrese, S., & Moscardini, L. 1998, *Mon. Not. R. Astron. Soc.*, 300, 747
Zehavi, I., Blanton, M. R., Frieman, J. A., et al. 2002, *Astrophys. J.*, 571, 172
Zehavi, I., Eisenstein, D. J., Nichol, R. C., et al. 2005, *Astrophys. J.*, 621, 22
Zehavi, I., Zheng, Z., Weinberg, D. H., et al. 2011, *Astrophys. J.*, 736, 59
Zucca, E., Bardelli, S., Bolzonella, M., et al. 2009, *Astron. Astrophys.*, 508, 1217

Appendix A: Covariance matrices

In this analysis, the errors on both the connected and reduced 3PCF are estimated from the diagonal elements of the covariance matrices, calculated using the 26 mocks discussed in Sect. 3.3. We have also estimated the full normalised covariance matrices, defined as:

$$C_{ij} = \frac{1}{N} \sum_{k=1}^N \left(\frac{Q_i^k - \bar{Q}_i}{\sigma_{Q_i}} \right) \left(\frac{Q_j^k - \bar{Q}_j}{\sigma_{Q_j}} \right), \quad (\text{A.1})$$

where σ_{Q_i} is the value of the covariance of the i -th elements. We show for illustrative purposes in Figs. A.1 and A.2 for the luminosity bins at two characteristic scales, $r_{12} = 2.5$ and $r_{12} = 10 h^{-1} \text{Mpc}$, respectively.

We find that at the smallest scales the covariance between bins is small, decreasing with increasing luminosity threshold. At the highest scales the correlation between bins is more significant, decreasing, also in this case, with increasing luminosity threshold, and presents a similar shape to the one obtained in other analysis (e.g. Gaztañaga & Scoccimarro 2005;

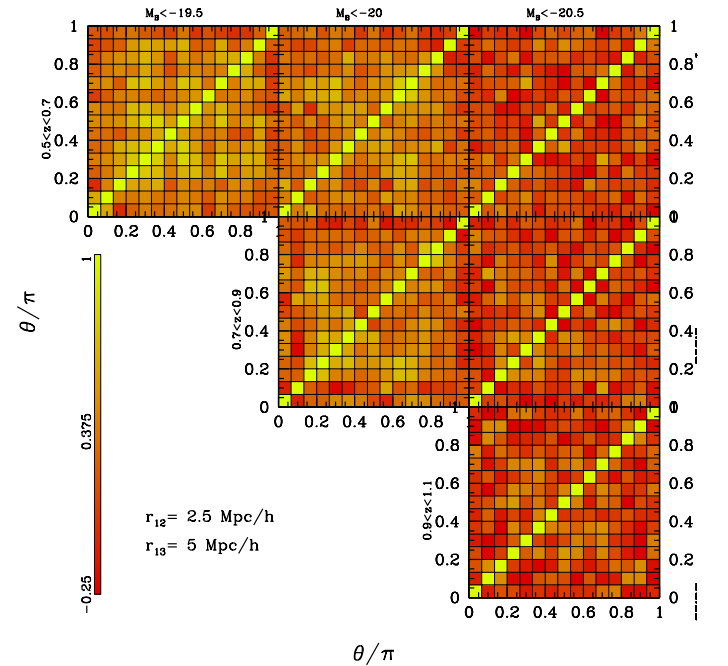


Fig. A.1. Normalised covariance matrices estimated at scales $r_{12} = 2.5 h^{-1} \text{Mpc}$ in the same luminosity and redshift bins as in Fig. 3.

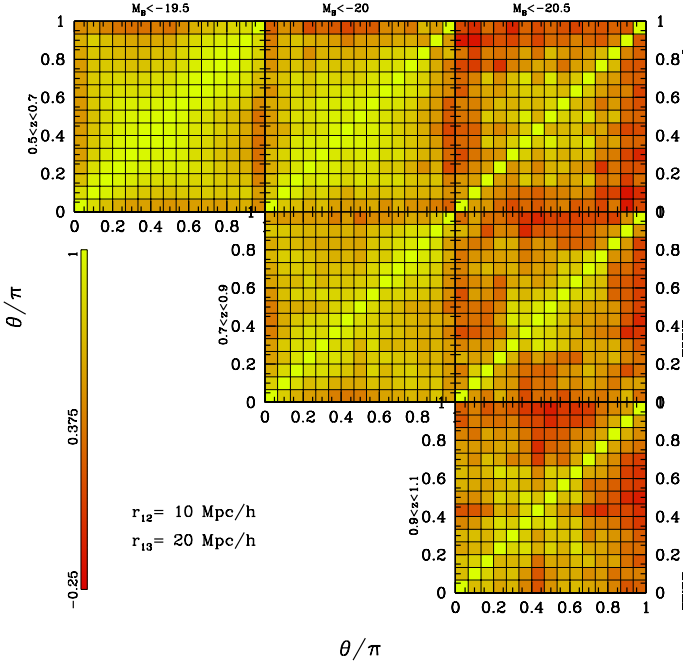


Fig. A.2. Same as Fig. A.1, but for scales $r_{12} = 10 h^{-1} \text{ Mpc}$.

Hoffmann et al. 2015). In this work, we have considered only the diagonal parts of the covariance matrix, given the small number of available mocks; while for the purpose of this paper this is not significant, and the main results and trends found are not affected by this assumption, their statistical significance might be, especially at the larger scales. In these cases, a statistical analysis of the data would require the use of the full covariance to correctly estimate errorbars. We plan to take it into account in a future analysis, in which we plan to provide constraints on the galaxy bias.

-
- ¹ Dipartimento di Fisica e Astronomia - Alma Mater Studiorum Università di Bologna, viale Berti Pichat 6/2, I-40127 Bologna, Italy
 - ² INAF - Osservatorio Astronomico di Bologna, via Ranzani 1, I-40127 Bologna, Italy
 - ³ INFN - Sezione di Bologna, viale Berti Pichat 6/2, I-40127 Bologna, Italy
 - ⁴ Dipartimento di Matematica e Fisica, Università degli Studi Roma Tre, via della Vasca Navale 84, 00146 Roma, Italy
 - ⁵ INFN - Sezione di Roma Tre, via della Vasca Navale 84, I-00146 Roma, Italy
 - ⁶ INAF - Osservatorio Astronomico di Roma, via Frascati 33, I-00040 Monte Porzio Catone (RM), Italy
 - ⁷ Laboratoire Lagrange, UMR7293, Université de Nice Sophia-Antipolis, CNRS, Observatoire de la Côte d'Azur, 06300 Nice, France
 - ⁸ Aix Marseille Université, CNRS, LAM (Laboratoire d'Astrophysique de Marseille) UMR 7326, 13388, Marseille, France
 - ⁹ INAF - Osservatorio Astronomico di Brera, Via Brera 28, 20122 Milano, via E. Bianchi 46, 23807 Merate, Italy
 - ¹⁰ Dipartimento di Fisica, Università di Milano-Bicocca, P.zza della Scienza 3, I-20126 Milano, Italy
 - ¹¹ INAF - Osservatorio Astronomico di Torino, 10025 Pino Torinese, Italy
 - ¹² Canada-France-Hawaii Telescope, 65–1238 Mamalahoa Highway, Kamuela, HI 96743, USA
 - ¹³ Aix Marseille Université, CNRS, CPT, UMR 7332, 13288 Marseille, France
 - ¹⁴ Université de Toulon, CNRS, CPT, UMR 7332, 83957 La Garde, France
 - ¹⁵ INAF - Istituto di Astrofisica Spaziale e Fisica Cosmica Milano, via Bassini 15, 20133 Milano, Italy
 - ¹⁶ Department of Astronomy, University of Geneva ch. d'Ecogia 16, CH-1290 Versoix, Switzerland
 - ¹⁷ INAF - Osservatorio Astronomico di Trieste, via G. B. Tiepolo 11, 34143 Trieste, Italy
 - ¹⁸ Institute of Physics, Jan Kochanowski University, ul. Swietokrzyska 15, 25-406 Kielce, Poland
 - ¹⁹ National Centre for Nuclear Research, ul. Hoza 69, 00-681 Warszawa, Poland
 - ²⁰ Institute d'Astrophysique de Paris, UMR7095 CNRS, Université Pierre et Marie Curie, 98 bis Boulevard Arago, 75014 Paris, France
 - ²¹ Astronomical Observatory of the Jagiellonian University, Orla 171, 30-001 Cracow, Poland
 - ²² Institute of Cosmology and Gravitation, Dennis Sciama Building, University of Portsmouth, Burnaby Road, Portsmouth, PO1 3FX, UK
 - ²³ INAF - Istituto di Astrofisica Spaziale e Fisica Cosmica Bologna, via Gobetti 101, I-40129 Bologna, Italy
 - ²⁴ INAF - Istituto di Radioastronomia, via Gobetti 101, I-40129 Bologna, Italy